Nanoscale

PAPER

View Article Online
View Journal | View Issue

Cite this: *Nanoscale*, 2025, **17**, 12775

Designing atomically precise gold nanocluster architectures with DNA-guided self-assembly and biofunctionalization approaches†

Abdallah Alhalabi,[a,b] Christine Saint-Pierre,[b] Elisabetta Boeri-Erba,[c] Pierre-Henri Elchinger,[b] Harinderbir Kaur,[c] Didier Gasparutto *[b] and Xavier Le Guével *[a]

Atomically precise gold nanoclusters (AuNCs) are nanomolecular species with unique optoelectronic properties, both at the individual and assembled levels. Herein, we demonstrate the precise ligand engineering of AuNCs, enabling the controlled grafting of single-stranded oligonucleotides onto atomically defined AuNCs of different sizes—Au_{18} and Au_{25}—which emit in the NIR-I (600–800 nm) and NIR-II (900–1300 nm) spectral windows, respectively. These biofunctionalized AuNCs, which can be considered nanomolecular building blocks, were thoroughly characterized using complementary analytical and optical techniques, including absorption and fluorescence spectroscopy, mass spectrometry, liquid chromatography, and gel electrophoresis. Through selective DNA hybridization, we successfully assembled AuNC dimers, trimers, and AuNC–dye nanosystems with high reproducibilities and yields. This work lays the foundation for the design of AuNC–DNA superstructures with potential applications in optoelectronics, sensing, and nanomedicine.

Received 28th February 2025,
Accepted 20th April 2025

DOI: 10.1039/d5nr00905g

rsc.li/nanoscale

Introduction

Atomically precise gold clusters (AuNCs) represent a promising class of nanomolecular species with a wide variety of applications in catalysis,[1] optoelectronics[2] and nanomedicine and notably in sensing,[3–5] imaging[6–8] and therapy.[9,10] AuNCs exhibit molecular-like properties, such as multiple absorption bands and tunable photoluminescence (PL), which are directly linked to the gold structure and the nature and coordination of ligands stabilizing the metal core. Some recent studies have also reported remarkable new optical and electronic properties of AuNCs when they were assembled either covalently or electrostatically through aggregation[11] or using short organic crosslinkers,[12] polymers,[13,14] metal–organic frameworks,[15] or biomolecules (siRNA[16,17] and proteins). Several recent reviews have reported the advances in this emerging field of research.[18–25]

However, while such nanostructures have been, to some extent, well-characterized experimentally and through theoretical models,[11,21,25–27] there is still a lack of a strategy to design these nanostructures *via* a bottom-up approach, coupled with analytical methods to determine their intermediary and final stoichiometric species.

DNA nanotechnology is considered one of the most suitable options to ensure the reproducible and well-controlled assembly of nanoparticles at different scales.[28] For instance, metal nanoparticles (gold, silver) or nanocrystals have been attached *via* post-functionalization at different distances following 1D, 2D, or 3D patterns.[29–32] The ability to either attach metal particles such as AuNCs or use AuNCs functionalized with oligonucleotides (ODNs) to initiate the formation of superstructures *via* self-assembly therefore seems an appropriate route.

In this work, we aimed to demonstrate how the fine control over the number of ODNs through ligand-exchange reactions on two well-described atomically precise AuNCs ($Au_{25}pMBA_{18}$ [33–35] and $Au_{18}SG_{14}$,[36,37] where pMBA is *para*-mercaptobenzoic acid and SG is glutathione) could enable the creation of a set of building blocks to further generate dimer and trimer nanostructures while modulating the distance between these nanomolecular species. Each step was confirmed through molecular techniques and optical and microscopy

[a]*Université Grenoble Alpes, INSERM U1209, CNRS UMR 5309, Institut pour l'Avancée des Biosciences (IAB), Cancer Targets & Experimental Therapeutics, 38000 Grenoble, France. E-mail: xavier.le-guevel@univ-grenoble-alpes.fr*
[b]*Univ. Grenoble Alpes, CEA, CNRS, SyMMES-UMR 5819, F-38000 Grenoble, France. E-mail: didier.gasparutto@cea.fr*
[c]*Univ. Grenoble Alpes, CEA, CNRS, IBS, F-38000 Grenoble, France*

†Electronic supplementary information (ESI) available: The physico-chemical and optical characterization of AuSG (S2), AupMBA (S3), AupMBA-N3 (S4) as well as PAGE and microscopy measurements of the AuNC-ODNs and AuNC dimer structures (S5–S11). See DOI: https://doi.org/10.1039/d5nr00905g

characterizations, demonstrating the high yield and selectivity of this DNA-guided approach for assembling biohybrid architectures.

Experimental section

Chemicals

Chemical products were purchased from Sigma-Aldrich (France). All oligonucleotides were purchased from Eurogentec, except for the bicyclononyne (BCN)-containing sequence, which was prepared in our laboratory *via* solid-phase synthesis[38,39] using the BCN phosphoramidite monomer (5′-click easy BCN II reagent from Biosearch Technologies). The thiol-dPEG$_5$-azido ($C_8H_{17}N_3O_3S$) linker was purchased from Biosynth.

Synthesis and purification of the $Au_{25}(pMBA)_{18}$ clusters

The clusters were prepared by a synthesis route adapted from Bertorelle *et al.*[40] Briefly, pMBA (5.1 mmol, 79 mg) was first dissolved in 40 mL of methanol and 4 mL of tributylamine. Then, tetrachloroauric acid trihydrate $HAuCl_4$ (2.54 mmol, 100 mg) was added at ambient conditions and the solution was stirred for 30 min to form a gold thiolate/tributylamine complex. Then, to induce a slow reduction of the gold, 200 mg of trimethylamine borane was added under stirring for 2 h before adding another 200 mg of the same. The solution was left stirring overnight for 24 h to achieve the formation of clusters. Precipitation of the clusters was induced by adding 1 mL of 10% NH_4OH solution and 30 mL of diethyl ether. After centrifugation, the supernatant, which contained unwanted products and residue, was removed. Another cycle of dissolution/precipitation (1 mL H_2O; 5 mL of MeOH and 20 mL of Et_2O) was then done. Purification of the $Au_{25}(pMBA)_{18}$ cluster was conducted by selective precipitation. The precipitate was dissolved in 5 mL of water, and then 700 mg of ammonium acetate was added, followed by 20 mL of MeOH. Under these conditions, a precipitate appears, which was then separated by centrifugation. This precipitate was essentially composed of $Au_{36}(pMBA)_{24}$ with good purity. $Au_{25}(pMBA)_{18}$ was soluble in the supernatant and could be precipitated by adding Et_2O. Two cycles of dissolution/precipitation were done to improve the purity of the end cluster, the last one using a minimum of water/MeOH precipitated by Et_2O. Finally, the pellet was dried overnight in air.

Synthesis and purification of the Au(SG) clusters

The clusters were prepared by a synthesis route adapted from Pyo *et al.*[41] In a typical synthesis, an aqueous solution of 20 mM $HAuCl_4$ (12.5 mL) and 50 mM glutathione (SG, 7.5 mL) was added to 230 mL of ultrapure water in a 500 mL Erlenmeyer flask (see the ESI† for the materials and methods). The mixture was then vigorously stirred for 2 min until the yellowish solution turned cloudy. Afterwards, the pH was adjusted to 12.0 using 1 M NaOH, which caused the color of the solution to turn clear yellow. Thereafter, 0.1 mL of diluted $NaBH_4$ (3.5 mM) was slowly added dropwise. The reaction solution was then stirred for 30 min. During the first 15 min, the solution slowly turned orange. Finally, the pH was adjusted to 2.5 to quench the BH_4^- activity and the solution was stirred slowly (150 rpm) for 6 h at room temperature. The product solution was then rotary evaporated to near dryness. To isolate Au(SG) from the raw product, solvent fractionation was conducted using water–isopropanol (IPA) mixtures. Typically, the product was dissolved in 10 mL of water, and 12 mL of IPA was added to induce the precipitation of large-sized nanoclusters, which contained different species, such as $Au_{22}(SG)_{18}$ in addition to smaller species ($Au_{10}SG_{10}$, $Au_{15}SG_{13}$ and $Au_{18}SG_{14}$). The precipitate was separated by centrifugation, and more IPA (1 mL) was added to the supernatant to induce the additional precipitation of Au(SG). This process was repeated until the supernatant was clear.

Biofunctionalization of the nanoclusters by ligand-exchange reactions

In the case of ODNs, ligand exchange was performed using thio-hexyl containing ODNs (with the HS-$(CH_2)_6$ linker inserted at the 3′-end, 5′-end or internal position). In typical conditions, 100 μL of AuNCs (100 μM) was mixed with 200 μL of ODN-SH (100 μM), and then the triethylammoniun acetate (TEAA) concentration was adjusted to 300 mM. The reaction solution was then incubated in an Eppendorf ThermoMixer at 40 °C with stirring at 600 rpm overnight. The resulting reaction mixture was analyzed and purified through PAGE and HPLC to separate the different AuNC(n)–ODN(n) species.

Ligand exchange was also performed using a thiol-dPEG5-azido ($C_8H_{17}N_3O_3S$) linker. Typically, for 100 μL of AuNCs (100 μM), 200 μL of thiol-dPEG$_5$-azido (200 μM) diluted in a 50% acetonitrile/water solution was added. Next, TEAA (1 M) was added to reach a final concentration of 300 mM. The reaction mixture was incubated in an Eppendorf ThermoMixer at 60 °C with stirring at 600 rpm overnight. The reaction was monitored by MALDI-ToF mass spectrometry and stopped once the desired distribution of N_3 on the NC was achieved. The $Au_{25}(pMBA)$–N_3 mixture was then purified by precipitation and analyzed by absorbance measurements and RP-HPLC.

Biofunctionalization of the nanoclusters by click reactions

In similar conditions to those used in the ligand exchange, 100 μL of azide-modified gold nanoclusters ($Au_{25}(pMBA)$–N_3) (100 μM) was mixed with 200 μL of 5′-BCN-ODN (100 μM). Next, TEAA was added to reach a final concentration of 300 mM. The reaction took place at room temperature overnight.

DNA hybridization

AuNCs biofunctionalized with single-stranded oligonucleotides were hybridized with their complementary strands with or without AuNCs or dye labeling by mixing both at similar concentrations, then raising the temperature to 75 °C for 5 min and finally allowing to cool down to room temperature in 1 h.

Native polyacrylamide gel electrophoresis (PAGE)

Native PAGE separation was carried out using a vertical gel electrophoresis unit and 19 : 1 acrylamide : bis(acrylamide) ratio. The separating gels were prepared with a final concentration of 25% to separate the sub-AuNC species and 20% to separate the AuNC–ODN subspecies. In all cases, a stacking gel with 3% concentration was prepared. The elution was done using standard TBE buffer (89 mM Tris, 89 mM boric acid, 2 mM EDTA) at a cool temperature. The AuNC and AuNC–ODN structures (20 μM) were dissolved in 20% (v/v) glycerol/TBE solution. The sample solutions were then loaded onto the stacking gel (25 μL per well) and eluted for 4 h at a constant voltage mode (150 V) to achieve sufficient separation. The gels were imaged either in the visible or NIR region by an ultraviolet gel documentation system (Gel Doc XR+ System, BioRad, USA) or in the SWIR optical window (900–1700 nm) according to the emission wavelength of the examined AuNCs.

NIR-II imaging

This was performed using a NIR-II Princeton camera 640ST (900–1700 nm) coupled with a laser excitation source at λ = 808 nm (100 mW cm^{-2}). A short-pass excitation filter was used at 1000 nm (Thorlabs) and a long-pass emission filter (LP) set at 1064 nm (Semrock) was coupled on to a 35 mm lens (Navitar, N.A. = 4).

Reverse phase high-pressure liquid chromatography (RP-HPLC)

RP-HPLC was used to analyze and purify the different AuNCs and AuNC–ODN conjugates. Typically, the purifications were performed by reverse phase HPLC using a C18 column (Uptisphere, 250 × 4.6 mm, 5 μm, 300 A) with a gradient of acetonitrile in 10 mM triethylammonium acetate buffer. The detection was performed by UV–visible absorbance measurements using a diode array detector from a series 1100 Agilent chromatographic system. After concentration of the collected fractions under vacuum, the samples were quantified by absorbance measurements using a microvolume spectrophotometer (Denovix ds-11). Then their purity and integrity were verified using an RP-HPLC system (Agilent Technologies, 1260 Infinity) coupled with an electrospray mass spectrometer (Agilent Technologies single quadrupole 6120). Here, 200 pmol was injected on to the column (Uptisphere C18, 150 × 2 mm, 3 μm, 300 Å) and eluted with a gradient of acetonitrile in triethylammonium acetate buffer (5 mM). Peaks corresponding to the multiple-charged ions were recorded in the range of 600–1100 m/z in the negative mode and the mass was calculated with a deconvolution algorithm.

Matrix-assisted laser desorption/ionization time-of-flight mass spectrometry (MALDI-ToF-MS)

The mass spectra were obtained in the negative mode on a time-of-flight Microflex mass spectrometer (Bruker, Wissembourg, France), equipped with a 337 nm nitrogen laser and pulsed delay source extraction system. The matrix was prepared by dissolving 3-hydroxypicolinic acid in 10 mM ammonium citrate buffer. A mixture of a purified DNA sample (10 pmol; 1 μL) was added to the matrix (1 μL) and spotted on a polished stainless steel target plate using the dried droplet method. The spectra were calibrated using reference oligonucleotides of known masses.

Native mass spectrometry (MS)

Native MS analysis was carried out on a quadrupole time-of-flight mass spectrometer (Q-TOF Ultima, Waters Corporation, Manchester, U.K.). Ions were generated using a nanoflow electrospray (nano-ESI) source. Nanoflow platinum-coated borosilicate electrospray capillaries were used (purchased from Thermo Electron SAS, Courtaboeuf, France). The following instrumental parameters were used: capillary voltage = 1.2–1.3 kV, cone potential = 40 V, RF lens-1 potential = 40 V, RF lens-2 potential = 1 V, aperture-1 potential = 0 V, collision energy = 30–140 V, and microchannel plate (MCP) = 1900 V. All the mass spectra were calibrated externally using a solution of cesium iodide (6 mg mL^{-1} in 50% isopropanol) and were processed using Masslynx 4.0 software (Waters Corporation, Manchester, U.K.).

Optical measurements

All the spectroscopic measurements were performed in 1 cm quartz cuvettes (Hellma GmbH) at room temperature using air-saturated solutions. The absorption spectra of the diluted AuNC and AuNC–ODN samples in water and in TEAA buffer (10 mM) were recorded using an Agilent Cary 300 UV–vis spectrophotometer between 190 and 800 nm. Steady-state photoluminescence spectra were measured from 500 to 800 nm on a Fluoromax (Perkin Elmer) spectrofluorometer and between 600 and 1750 nm with a calibrated FSP 920 spectrofluorometer (Edinburgh Instruments, Edinburgh, United Kingdom) equipped with a nitrogen-cooled PMT R5509P. Determination of the PL emission enhancement was estimated using the area under each curve using GraphPad Prism software.

Transmission electron microscopy (TEM)

Around 3 μL of AuNC solution was deposited onto an ultrathin carbon film or graphene support film. Imaging was performed on a Thermo Fisher Tecnai F20 TEM system operating at 200 kV. Data were collected on a Ceta detector (4k × 4k).

High-resolution transmission electron microscopy (HRTEM)

The metal core sizes were determined by HRTEM with a 200 kV monochromated TEM instrument using dispersed Au NCs on ultrafine carbon films.

Scanning transmission electron microscopy (STEM)

The nanostructures were imaged with the STEM mode using a Zeiss Merlin microscope. Images were collected using both bright field and dark field detectors at 30 kV with a beam current of 250 pA with magnifications between 2× and 200k×.

List of DNA sequences used in this study

The structures of linkers and dye monomers are shown in the ESI (see Fig. S1†)

Name	Sequence
5′-(Thiol)-5mer	5′ (Thiol-C6)-CAC-GT 3′
17mer	5′ ACA-TTC-CTA-AGT-CTG-AA 3′
17mer complementary	5′ TTC-AGA-CTT-AGG-AAT-GT 3′
5′-(Thiol)-17mer	5′ (Thiol-C6)-ACA-TTC-CTA-AGT-CTG-AA 3′
5′-(Thiol)-17mer complementary	5′ (Thiol-C6)-TTC-AGA-CTT-AGG-AAT-GT 3′
17mer complementary-(Thiol)-3′	5′ ACA-TTC-CTA-AGT-CTG-AA-(C6-Thiol) 3′
17-mer (internal Thiol) complementary	5′ TTC-AGA-CT-(Thiol-C6) dT-AGG-AAT-GT 3′
5′-(Cy3)-17-mer	5′ (Cy3)-ACA-TTC-CTA-AGT-CTG-AA 3′
5′-(BCN)-15-mer	5′ (BCN)-TGA-ACT-GCA-GCT-CCT 3′

Results and discussion

$Au_{25}(pMBA)_{18}$ and $Au_{18}(SG)_{14}$ were synthesized following protocols established in the literature.[1] These syntheses approaches led to high yields of atomically precise AuNCs, although with some size heterogeneity, as observed by PAGE (Fig. 1A and Fig. S2A†). In the literature, several approaches have been applied to isolate a single atomically precise size with high purity, such as selective precipitation and polyacrylamide gel electrophoresis (PAGE).[42] However, while PAGE offers high resolution and purity, it is time-consuming and requires multiple washing steps to remove acrylamide, often resulting in relatively low AuNC yields. Therefore, we opted for an alternative approach based on reverse-phase high-pressure liquid chromatography (RP-HPLC) to separate atomically precise AuNCs.

The choice of solvent gradient is critical for the efficient separation of AuNC species and depends on the nature of the ligands stabilizing the gold core—in this case, pMBA and SG. Here, crude reaction mixtures of $Au_{25}(pMBA)_{18}$ (50 μL, 10 μM) were injected into an RP-HPLC system equipped with a UV–visible absorbance detector, with a linear acetonitrile gradient from 2% to 20%, in 10 mM TEAA buffer. Atomically precise AuNCs were then separated based on differences in their retention time related to their molecular weight, polarity, and hydrophobicity (Fig. 1A). The isolated AuNCs were identified according to their known absorbance signatures reported in the literature[40,43–45] and were confirmed by mass spectrometry to be respectively: $Au_{36}(pMBA)_{24}$, $Au_{25}(pMBA)_{18}$, $Au_{28}(pMBA)_{20}$ and $Au_{10}(pMBA)_{10}$ (Fig. 1B and Fig. S3†). For instance, $Au_{25}(pMBA)_{18}$ showed the typical absorption bands of this species at 370, 450, 480, 690, and 800 nm.[34]

The glutathione-stabilized AuNCs were purified in a similar manner, but using a lower acetonitrile gradient than for Au(pMBA) to enable the separation and extraction of three species, namely $Au_{15}(SG)_{13}$, $Au_{18}(SG)_{14}$ and $Au_{22}(SG)_{18}$ (Fig. S2A and B†), with their compositions assigned based on their absorbance profiles[46] (Fig. S2C†) and ESI mass spectrometry data (data not shown).

$Au_{25}(pMBA)_{18}$ and $Au_{18}(SG)_{14}$ were chosen for the following experiments. The composition of the $Au_{25}(pMBA)_{18}$ was confirmed by MALDI-ToF MS measurements with a major peak at 7681.1 Da (theoretical mass = 7681.3), but with additional peaks corresponding to $Au_{25}(pMBA)_{17}$ and $Au_{25}(pMBA)_{16}$ detected (−1 or −2 pMBA) either due to mild fragmentation during ionization or due to the presence of these subspecies in the sample (Fig. 1C). These AuNCs exhibited broad photoluminescence (PL) emission in the NIR-II window under infrared excitation ($\lambda_{exc.}$ 808 nm) (also known as shortwave infrared, SWIR), with a maximum at around 1100 nm (Fig. 1D). The HRTEM image depicted in Fig. 1E confirmed their ultrasmall size (<2 nm) and semi-crystalline structure with atomic precision.

The composition of $Au_{18}(SG)_{14}$ was also confirmed by native MS analysis (Fig. S2D†), with sizes smaller than 2 nm observed by HRTEM (Fig. S2E†). $Au_{18}(SG)_{14}$ exhibited PL in the NIR-I window with a maximum at 680 nm ($\lambda_{exc.}$ 450 nm) (Fig. S2F†).

Oligonucleotide functionalization

To biofunctionalize atomically precise AuNCs with DNA strands, two strategies were tested: (1) azide functionalization of the AuNC surface *via* ligand exchange, followed by ODN binding through click chemistry, and (2) direct ligand exchange with thiol-modified ODNs on the AuNC surface.

In the first approach, $Au_{25}pMBA_{18}$ was initially modified with a short pegylated thiol linker (thiol-PEG_3-N_3). The reaction was stopped after 24 h in order to prevent the broad distribution of this linker on the AuNC surface from 5 to 17 PEG_3-N_3 (data not shown). MALDI-ToF mass spectrometry indicated a distribution from 1 to 4 PEG_3-N_3 ligands per AuNC (Fig. S4A†) with no changes in the absorbance spectrum (Fig. S4B†), indicating the conservation of the Au_{25} structure.[46] RP-HPLC analysis of $Au_{25}(pMBA)$–N_3 showed that the azide-functionalized AuNCs were more hydrophobic and less polar due to the presence of the N_3 group, resulting in longer retention times (Fig. S4C†). Subsequently, a click reaction was carried out (see methods) with $Au_{25}(pMBA)$–N_3 and BCN-15mer, resulting in the successful conjugation, as observed by PAGE, which revealed three distinct new bands (Fig. S5†).

While this method provided relatively good stoichiometric control of the azide groups per AuNC, the long experimental setup (ligand exchange + click reaction) led us to pursue the second conjugation approach by direct ligand exchange with a thiol-modified ODN. By controlling the reaction stoichiometry and applying purification methods, we were able to graft a defined number of ODNs onto both $Au_{25}(pMBA)_{18}$ and $Au_{18}(SG)_{14}$. We further applied different oligonucleotides with different numbers of nucleobases (5mer and 17mer), with thiol modification on the 5′ or 3′ terminal of the ODNs or on any internal nucleobase.

By tuning the initial ratio of thiol-ODNs to AuNCs, it was possible to obtain species with a stoichiometric number of ODNs on the AuNC surface. Although RP-HPLC could not

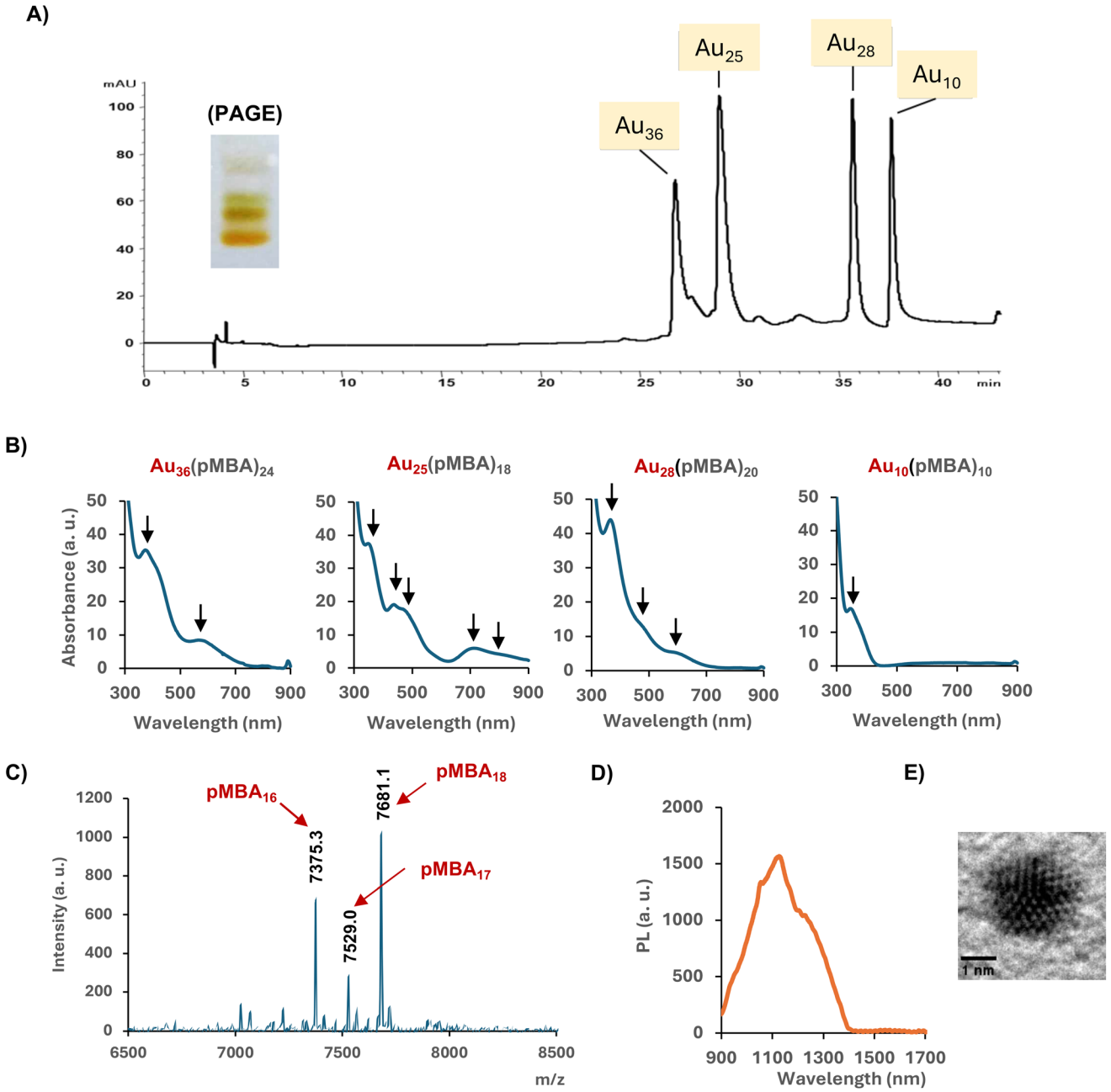

Fig. 1 (A) RP-HPLC analysis coupled with absorbance measurements for the $Au_{25}pMBA_{18}$ crude reaction mixture, eluted on a gradient from 0% to 20% acetonitrile in 10 mM TEAA buffer, showing different AuNC subspecies eluted at different retention times; inset shows a photograph from PAGE analysis of the same Au(pMBA) crude reaction mixture. (B) Corresponding absorbance spectra of each eluted subspecies. (C) MALDI-ToF MS spectrum of purified $Au_{25}pMBA_{18}$. (D) NIR-II PL spectrum of $Au_{25}pMBA_{18}$ dispersed in water; $\lambda_{exc.}$ = 808 nm. (E) HRTEM image of $Au_{25}pMBA_{18}$.

effectively resolve the individual species in the $Au_{25}(pMBA)_{18}$–$ODN_{(n)}$ conjugates, PAGE analysis revealed three nicely distinguished bands that exhibited the NIR-II luminescence of the separated subspecies of $Au_{25}(pMBA)_{(18-n)}$-$5mer_{(n)}$ (Fig. 2A). The molecular composition of each band was determined by MALDI-ToF-MS and the results confirmed the replacement of pMBA ligands by thiol-5mer ODNs with $Au_{25}(pMBA)_{(18-n)}$-$5mer_{(n)}$ (n = 0, 1, 2) + 1501 + 3000 (Fig. 2B), where (+1504 m/z and 3008 m/z) correspond to the mass of one thiol-5mer subtracted by the mass of one pMBA ligand and the mass of two thiol-5mers subtracted by the mass of two pMBA ligands, respectively.

To evaluate the efficiency of conjugation with longer ODNs suitable for hybridization (15-mer minimum to provide stable hybridization with the complementary strand), a similar experiment was performed with $Au_{25}(pMBA)_{18}$ using a terminal thiol-modified 17-mer and its complementary sequence, as well as a 17-mer with the thiol group positioned in the

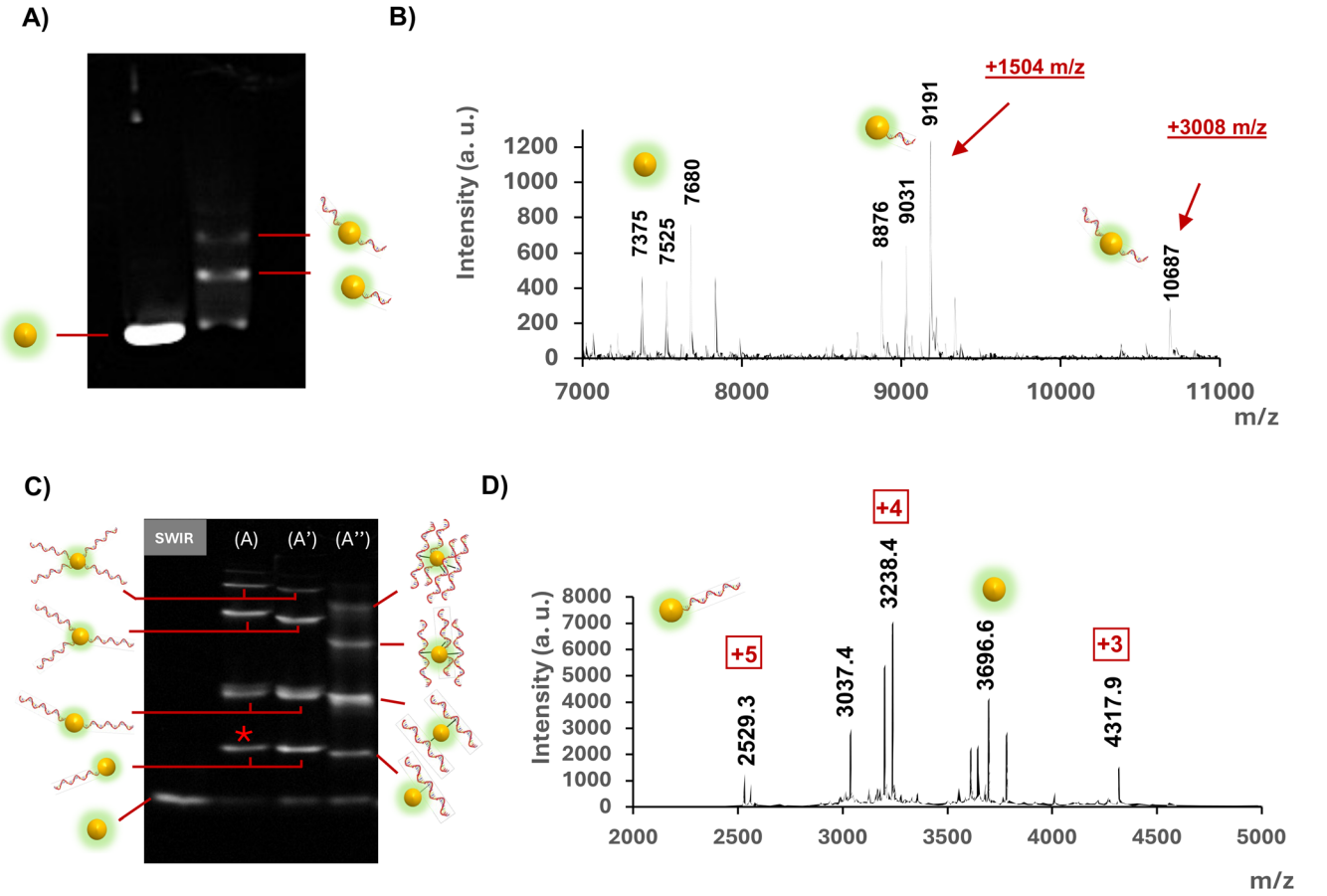

Fig. 2 (A) Native PAGE analysis of the ligand-exchange reaction mixture of $Au_{25}(pMBA)_{18}$ conjugated with thiol-5mer; the original gel is shown in Fig. S6.† (B) MALDI-ToF mass spectrometry of the ligand-exchange reaction of $Au_{25}(pMBA)_{18}$ with thiol-5mer. (C) Native PAGE analysis of $Au_{25}(pMBA)_{18}$ conjugated with thiol-17mer (A), its complementary strand thiol-17mer (A'), and with the thiol (mid sequence)-17mer (A''); the original gel is shown in Fig. S7.† (D) Native ESI-MS for $Au_{25}(pMBA)_{18}$ grafted with a single thiol-17mer (red asterisk).

middle of the sequence. The gel bands of $Au_{25}(pMBA)_{(18-n)}$-$17mer_{(n)}$ revealed four bands with similar migration using either the thiol-17mer (Fig. 2C, lane A) or the complementary sequence thiol-17mer (Fig. 2C lane A'), as expected. Interestingly, four bands with slightly faster migration were observed when using the 17-mer sequence containing the thiol in the middle of the sequence (Fig. 2C lane A''). It should be noted that almost no band corresponding to the free $Au_{25}(pMBA)_{18}$ was observed in column A, A', A'' in PAGE, suggesting the efficient ligand exchange of the thiol-ODN with the AuNCs. The first band corresponding to $Au_{25}(pMBA)_{18}$ with a single 17-mer (Fig. 2C, lane A) was cut and then extracted. Native ESI-MS (nano-spray) measurements in the positive mode (Fig. 2D) suggested the presence of $Au_{25}(pMBA)_{17}$-$17mer_{(1)}$ species with +3, +4 and +5 ionization charges. We could also still observe free $Au_{25}(pMBA)_{18}$ and $Au_{25}(pMBA)_{16}$-$17mer_{(2)}$, indicating a possible post-ligand exchange reaction, or a re-organization of the structure during the extraction of the gel due to its low stability.

These results demonstrate that $Au_{25}(pMBA)_{(18-n)}$ nanoclusters with one, two, three, or four 17-mer ODNs could be obtained by adjusting the AuNC-to-ODN ratio. Although species with more than four ODNs per AuNC could be generated using different ratios, a higher number of ODNs can lead to increased heterogeneity, resulting in overlapping gel bands and reduced resolution. However, since resolving these higher-order species was not the objective of this study, they were excluded from further analysis.

To demonstrate the universality of this approach, the ligand-exchange reaction was applied to another AuNC, namely $Au_{18}(SG)_{14}$. A lower concentration of thiol-17mer was used compared to the experiment with $Au_{25}(pMBA)_{18}$ to target the formation of the monosubstituted $Au_{18}(SG)_{13}$-$17mer_{(1)}$. RP-HPLC coupled with absorbance spectroscopy was conducted to separate the different species (Fig. 3A). The top of this figure shows the RP-HPLC analysis of thiol-17mer, which was eluted at 36.4 min. The bottom of this figure shows the results for the analysis of the ligand-exchange reaction mixture, where it can be seen that the peak for the free thiol-17mer completely disappeared, indicating the complete ligand exchange between the glutathione ligand and the thiol-17mer. Two species could be isolated here: monosubstituted $Au_{18}(SG)_{13}$-$17mer_{(1)}$ (26.5 min), and

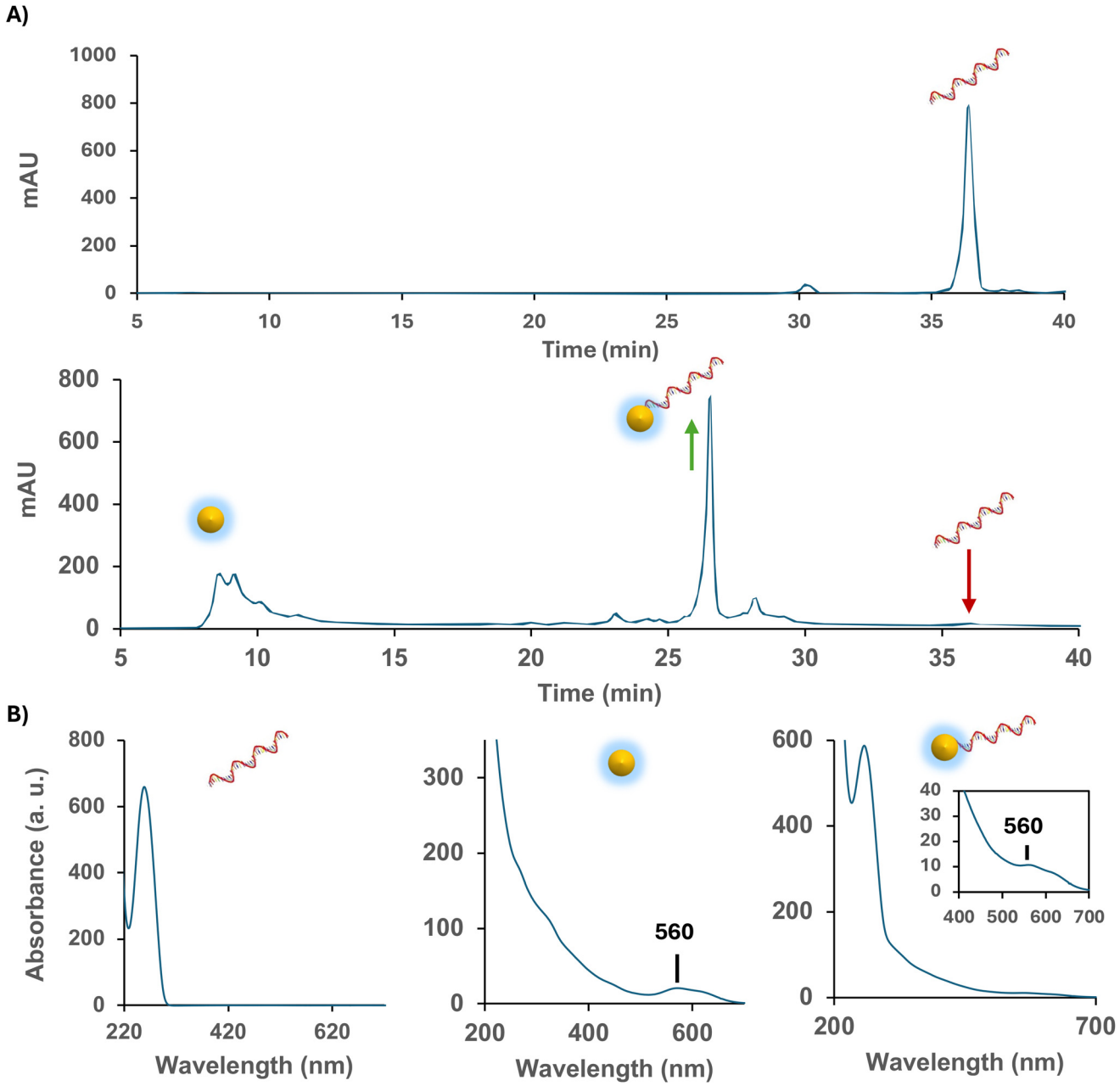

Fig. 3 (A) Top shows the RP-HPLC analysis for thiol-17mer, while the bottom shows the RP-HPLC analysis for $Au_{18}(SG)_{14}$ conjugated with thiol-17mer with a linear gradient from 0% to 12% of acetonitrile in 10 mM TEAA, and detection at 260 nm. (B) Corresponding absorbance measurements of the three peaks assigned to thiol-17mer, $Au_{18}(SG)_{14}$, and $Au_{18}(SG)_{13}$-$17mer_{(1)}$.

$Au_{18}(SG)_{14}$ in excess at 9.2 min. The UV–visible absorbance spectra of these 3 species (Fig. 3B) confirmed the efficient and controlled ligand exchange on the AuNCs stabilized either by the pMBA or SG ligand.

DNA hybridization and control of the nanostructures

Gold nanoclusters coupled with a controlled number of oligonucleotides could be used as the building bricks for many nano-architectures. This would pave the way for numerous applications requiring precise, quantitative measurement and analysis.

As a proof of concept, an experiment was performed to control the distance between single NIR-II emitting AuNCs and an orange emitting organic dye (Cy_3). $Au_{25}(pMBA)_{17}$-5′-$17mer_{(1)}$ or $17mer_{(1)}$-3′-$Au_{25}(pMBA)_{17}$ were hybridized with their complementary strand labeled with Cy3 dye on the 5′ end (5′-Cy3-17mer). Two possible double helix constructs were formed, with the distance between the AuNC and Cy3 being approximately 0 nm when they were on the same side or approximately 6 nm when they were on opposite sides. PAGE analysis of the two constructs and controls (5′-Cy3-17mer, $Au_{25}(pMBA)_{18}$, and double helix-Cy3) was performed by NIR-II

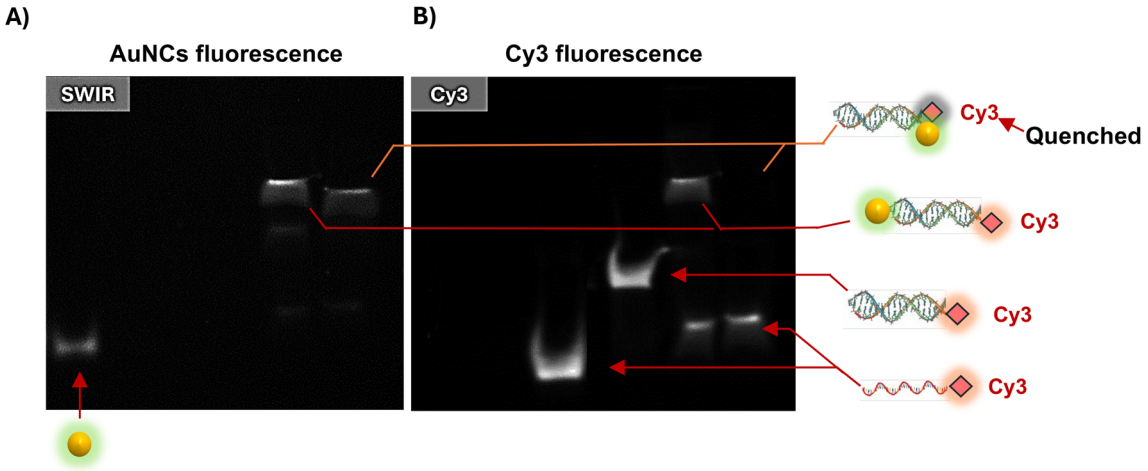

Fig. 4 Native PAGE analysis of the coupling between Cy3 dye and AuNCs through DNA hybridization (17-mer). Gel imaging was recorded using an NIR-II camera (A) and a BioRad gel imager with a Cy3 filter (B). The original gel is shown in Fig. S8.†

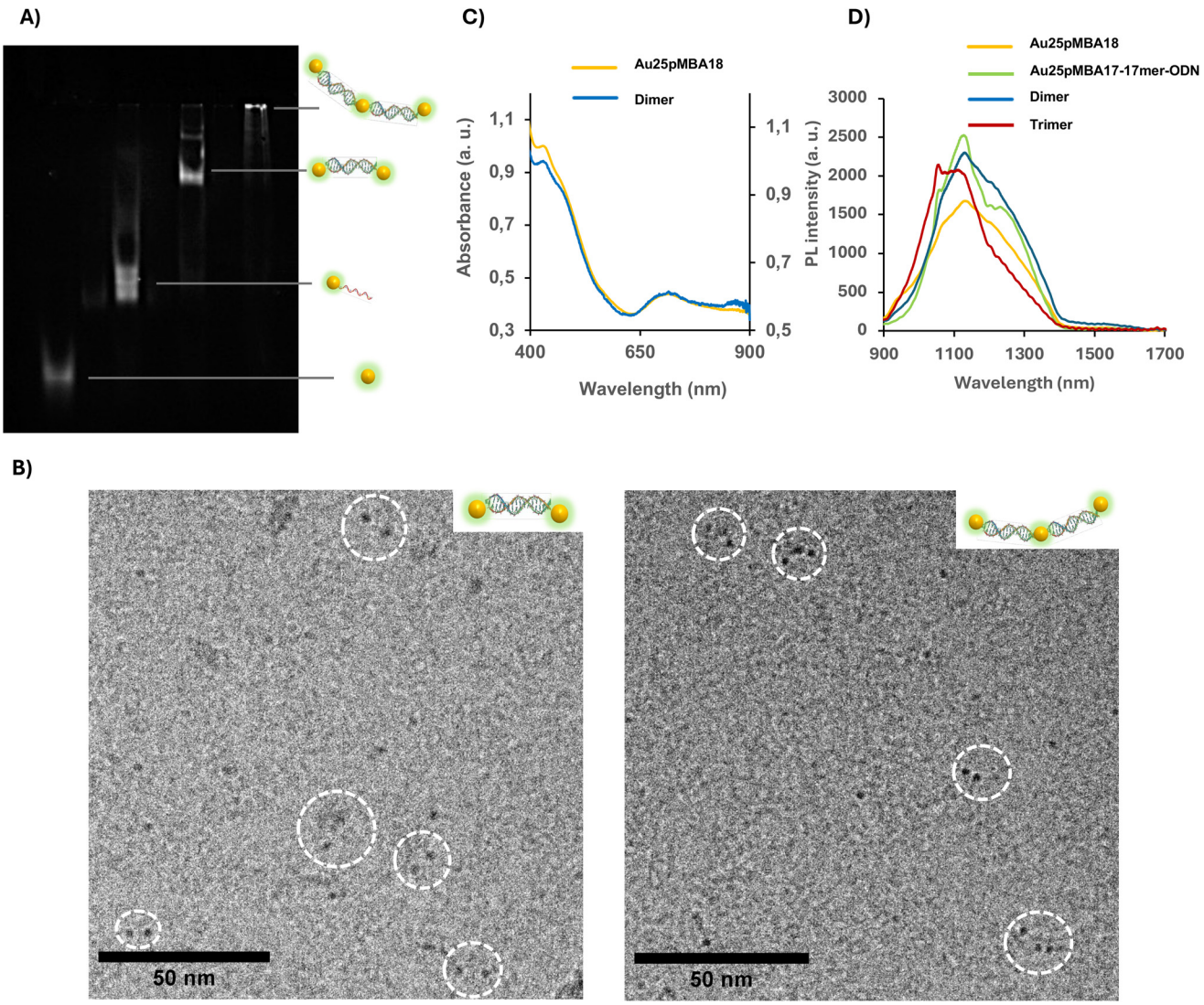

Fig. 5 (A) Native PAGE analysis of the hybridization reaction resulting in the Au_{25}(pMBA)-17mer dimer and trimer structures, image was taken using an NIR-II camera; the original gel is shown in Fig. S11.† (B) Absorbance and (C) PL spectra of dimers in comparison with free AuNCs dispersed in water; $\lambda_{exc.}$ 808 nm. (D) TEM images of the Au_{25}(pMBA)-17mer dimer and trimer structures.

imaging (Fig. 4A) and by red imaging (Fig. 4B). The double helix structures showed slower migration than the free AuNCs. Double helix-Cy3 showed only red emission with a higher molecular weight than 5′-Cy3-17mer. As expected, the two constructs with the double-helix structure AuNC–Cy3 at 0 and 6 nm distance showed similar migrations (*i.e.*, same molecular weight), which were higher than that of the double helix-Cy3. Interestingly, while both red and NIR-II emissions were detected with AuNC–Cy3 at 6 nm, only NIR-II emission was detected for AuNC–Cy3 at the 0 nm distance, whereby the red emission was fully quenched. For instance, Pyo *et al.* demonstrated the ability to use $Au_{25}(pMBA)_{18}$ as a pH sensor by quenching the fluorescent azadioxatriangulenium dye.[47] This implies that AuNCs, like any gold nanoparticles, are good quenchers when the organic dye is located in close proximity to the AuNC surface.[47,48]

With the library of AuNCs–ODNs in hand acting as nanomolecular building bricks, we intended to generate AuNCs dimers and trimers with high yields. We achieved this by the DNA hybridization of 17mer with AuNCs from one single ODN per AuNC and the same structure as the complementary ODNs (dimers) and from two ODNs per AuNC with a complementary single ODN per AuNC (trimers). Briefly, 5′-$Au_{25}(pMBA)_{17}$-$17mer_{(1)}$ (A) (10 μM) was hybridized with the complementary 5′-$Au_{25}pMBA_{17}$-17mer (A′) (10 μM) (dimers) and 5′-$Au_{25}(pMBA)_{16}$-$17mer_2$ (A′) (5 μM) was hybridized with two complementary 17mer (A′) with AuNCs on the 5′ end. The self-assembled dimer and trimer structures resulted in distances around 7 nm between the centers of the AuNCs, considering the ODN sequence. The PAGE analysis in Fig. 5A shows bands for the AuNCs alone, the AuNCs coupled with one ODN, dimers, and trimers, which were well-separated. The lower migration of the dimers and trimers, their sharp bands and the absence of unreacted 5′-$Au_{25}(pMBA)_{17}$-$17mer_{(1)}$ indicated the complete hybridization without the formation of extra species or aggregates. We then cut the bands related to the dimers and the trimers, washed them and resuspend them in water to determine their morphology and their optical properties. The TEM images in Fig. 5D suggest the presence of dispersed dimers and trimers. The observation of such structures is quite challenging, especially considering the sample preparation in the presence of salt, the low contrast of DNA and the ultrasmall size of the Au NCs. However, we were able to confirm the presence of a high number of dimers under mild conditions by STEM (Fig. S9†) despite the low resolution of the instrument. A total of 83 dimers and 14 trimers were observed in the TEM images, each with an intercluster distance of less than 7 nm, which was in agreement with the theoretical size of the double-stranded 17-mer at 5.78 nm. The absorbance spectrum of the AuNC dimers was similar to that of the single AuNCs, with the same specific absorption bands, indicating there had been no modification of the structure of the metal nanoclusters (Fig. 5B). The PL spectra showed a rather small enhancement around 1.4-fold when $Au_{25}(pMBA)_{18}$ had one ODN, with no significant changes observed when hybridized in dimers or trimers (Fig. 5C). This could be explained by the rather long distance (>5 nm) between AuNCs, which prevented efficient energy transfer. Moreover, this assembly was too small to collective induce an aggregation-induced fluorescence (AIE) effect,[49–51] and so the slight increase in the PL intensity might be related to the increase in the rigidity of the AuNCs in the dimers, therefore reducing the nonradiative process.[11–13]

A similar experiment was performed using 5′-$Au_{18}(SG)_{13}$-$17mer_{(1)}$ and either the free complementary 17mer or when linked to the AuNCs. PAGE analysis showed the good selectivity and efficient hybridizations with NIR emitting bands at lower migration, thus validating the nanostructuring approach with a different type of AuNCs (Fig. S10†).

Conclusion

In summary, we present a ligand-exchange-based method for precisely controlling the number of various ODNs on atomically precise gold nanoclusters (AuNCs) to create nanomolecular building blocks. Several analytical techniques, notably RP-HPLC coupled with absorbance and mass spectrometry, confirmed the hybridization of the 'AuNC–DNA blocks' into dimeric and trimeric biohybrid structures, as well as the formation of high-purity AuNC–dye nanosystems. We anticipate that this work will pave the way for new gold nanocluster architectures with DNA-guided self-assembly, offering potential applications in optoelectronics, sensing, and nanomedicine.

Author contributions

The manuscript was written through contributions of all the authors. All the authors have given approval for the final version of the manuscript.

Data availability

All the raw data related to the physico-chemical, analytical, optical characterizations will be available upon request from the two corresponding authors: Dr Xavier Le Guével (xavier.leguevel@univ-grenoble-alpes.fr) and Dr Didier Gasparutto (didier.gasparutto@cea.fr).

Conflicts of interest

There are no conflicts to declare.

Acknowledgements

This research project is financially supported by the Grenoble Alpes University (CBH-EUR-GS, ANR-17-EURE-0003 and Labex ARCANE, ANR-11-LABX-003) and the French Agence Nationale de la Recherche (project SIREN-ANR-20-CE92-0039, project

NanoGold – ANR-22-CE29-0022). D. G. is grateful to the French Alternative Energies and Atomic Energy Commission (CEA PTC-PE research program, MultiMASS project) that supported part of this study. H. K. acknowledges the financial support of the Cross-Disciplinary Program on Instrumentation and Detection of CEA, the French Alternative Energies and Atomic Energy Commission (CEA PTC-ID LCTEM). This work used the platforms of the Grenoble Instruct-ERIC center (ISBG; UAR 3518 CNRS-CEA-UGA-EMBL) within the Grenoble Partnership for Structural Biology (PSB) supported by FRISBI (ANR-10-INBS-05-02) and Labex GRAL (CBH-EUR-GS, ANR-17-EURE-0003). The IBS Electron Microscope facility is supported by the Auvergne–Rhône–Alpes Region, the Fonds Feder, the Fondation pour la Recherche Médicale and GIS IBiSA. The authors would like to thank Wai Li Ling and Laetitia Rapenne for the TEM and HRTEM characterizations.

References

1 S. Li, X. Du, Z. Liu, Y. Li, Y. Shao and R. Jin, Size Effects of Atomically Precise Gold Nanoclusters in Catalysis, *Precis. Chem.*, 2023, **1**(1), 14–28.
2 L. Chen, A. Black, W. J. Parak, C. Klinke and I. Chakraborty, Metal nanocluster-based devices: Challenges and opportunities, *Aggregate*, 2022, **3**(4), e132.
3 Y. Xiao, Z. Wu, Q. Yao and J. Xie, Luminescent metal nanoclusters: Biosensing strategies and bioimaging applications, *Aggregate*, 2021, **2**(1), 114–132.
4 L. Shang, S. Brandholt, F. Stockmar, V. Trouillet, M. Bruns and G. U. Nienhaus, Effect of Protein Adsorption on the Fluorescence of Ultrasmall Gold Nanoclusters, *Small*, 2012, **8**(5), 661–665.
5 I. M. Khan, S. Niazi, L. Yue, Y. Zhang, I. Pasha, M. K. Iqbal Khan, W. Akhtar, A. Mohsin, M. F. J. Chughati and Z. Wang, Research update of emergent gold nanoclusters: A reinforced approach towards evolution, synthesis mechanism and application, *Talanta*, 2022, **241**, 123228.
6 N. Sharma, W. Mohammad, X. Le Guével and A. Shanavas, Gold Nanoclusters as High Resolution NIR-II Theranostic Agents, *Chem. Biomed. Imaging*, 2024, **2**(7), 462–480.
7 C. Zhang, X. Gao, W. Chen, M. He, Y. Yu, G. Gao and T. Sun, Advances of gold nanoclusters for bioimaging, *iScience*, 2022, **25**(10), 105022.
8 D. Mordini, A. Mavridi-Printezi, A. Menichetti, A. Cantelli, X. Li and M. Montalti, Luminescent Gold Nanoclusters for Bioimaging: Increasing the Ligand Complexity, in *Nanomaterials*, 2023, vol. 13.
9 E. Porret, X. Le Guével and J. L. Coll, Gold Nanoclusters for Biomedical Applications: Toward In Vivo Studies, *J. Mater. Chem. B*, 2020, **8**, 2216–2232.
10 S. Mussa Farkhani, P. Dehghankelishadi, A. Refaat, D. Veerasikku Gopal, A. Cifuentes-Rius and N. H. Voelcker, Tailoring gold nanocluster properties for biomedical applications: From sensing to bioimaging and theranostics, *Prog. Mater. Sci.*, 2024, **142**, 101229.
11 Z. Wu, Y. Du, J. Liu, Q. Yao, T. Chen, Y. Cao, H. Zhang and J. Xie, Aurophilic Interactions in the Self-Assembly of Gold Nanoclusters into Nanoribbons with Enhanced Luminescence, *Angew. Chem., Int. Ed.*, 2019, **58**(24), 8139–8144.
12 T. M. Lahtinen, E. Hulkko, K. Sokołowska, T.-R. Tero, V. Saarnio, J. Lindgren, M. Pettersson, H. Häkkinen and L. Lehtovaara, Covalently linked multimers of gold nanoclusters Au102(p-MBA)44 and Au~250(p-MBA)n, *Nanoscale*, 2016, **8**(44), 18665–18674.
13 A. Yahia-Ammar, D. Sierra, F. Mérola, N. Hildebrandt and X. Le Guével, Self-Assembled, Gold Nanoclusters for Bright Fluorescence Imaging and Enhanced Drug Delivery, *ACS Nano*, 2016, **10**(2), 2591–2599.
14 N. Goswami, Q. Yao, Z. Luo, J. Li, T. Chen and J. Xie, Luminescent Metal Nanoclusters with Aggregation-Induced Emission, *J. Phys. Chem. Lett.*, 2016, **7**(6), 962–975.
15 Y. Nie, X. Tao, H. Zhang, Y.-Q. Chai and R. Yuan, Self-Assembly of Gold Nanoclusters into a Metal–Organic Framework with Efficient Electrochemiluminescence and Their Application for Sensitive Detection of Rutin, *Anal. Chem.*, 2021, **93**(7), 3445–3451.
16 S. Moro, M. Omrani, S. Erbek, M. Jourdan, C. I. Vandekerckhove, C. Nogier, L. Vanwonterghem, M.-C. Molina, P. Bernadó, A. Thureau, *et al.*, Self-Assembled Peptide-Gold Nanoclusters with SiRNA Targeting Telomeric Response to Enhance Radiosensitivity in Lung Cancer Cells, *Small Sci.*, 2024, 2400156.
17 Y. Lei, L. Tang, Y. Xie, Y. Xianyu, L. Zhang, P. Wang, Y. Hamada, K. Jiang, W. Zheng and X. Jiang, Gold nanoclusters-assisted delivery of NGF siRNA for effective treatment of pancreatic cancer, *Nat. Commun.*, 2017, **8**(1), 15130.
18 R. Antoine, Supramolecular Gold Chemistry: From Atomically Precise Thiolate-Protected Gold Nanoclusters to Gold-Thiolate Nanostructures, in *Nanomaterials*, 2020, vol. 10.
19 H. Chen, L. Zou, E. Hossain, Y. Li, S. Liu, Y. Pu and X. Mao, Functional structures assembled based on Au clusters with practical applications, *Biomater. Sci.*, 2024, **12**(17), 4283–4300.
20 J. V. Rival, P. Mymoona, K. M. Lakshmi, N. Nonappa, T. Pradeep and E. S. Shibu, Self-Assembly of Precision Noble Metal Nanoclusters: Hierarchical Structural Complexity, Colloidal Superstructures, and Applications, *Small*, 2021, **17**(27), 2005718.
21 S. Bonacchi, S. Antonello, T. Dainese and F. Maran, Atomically Precise Metal Nanoclusters: Novel Building Blocks for Hierarchical Structures, *Chem. – Eur. J.*, 2021, **27**(1), 30–38.
22 J. Wang, P. Li, C. Wang, N. Liu and D. Xing, Molecularly or atomically precise nanostructures for bio-applications: how far have we come?, *Mater. Horiz.*, 2023, **10**(9), 3304–3324.
23 S. Kolay, D. Bain, S. Maity, A. Devi, A. Patra and R. Antoine, Self-Assembled Metal Nanoclusters: Driving Forces and Structural Correlation with Optical Properties, in *Nanomaterials*, 2022, vol. 12.

24 A. Nag and T. Pradeep, Assembling Atomically Precise Noble Metal Nanoclusters Using Supramolecular Interactions, *ACS Nanosci. Au*, 2022, **2**(3), 160–178.
25 H. Li, X. Kang and M. Zhu, Superlattice Assembly for Empowering Metal Nanoclusters, *Acc. Chem. Res.*, 2024, **57**(21), 3194–3205.
26 W. S. Compel, O. A. Wong, X. Chen, C. Yi, R. Geiss, H. Häkkinen, K. L. Knappenberger Jr. and C. J. Ackerson, Dynamic Diglyme-Mediated Self-Assembly of Gold Nanoclusters, *ACS Nano*, 2015, **9**(12), 11690–11698.
27 Q. Yao, X. Yuan, Y. Yu, Y. Yu, J. Xie and J. Y. Lee, Introducing Amphiphilicity to Noble Metal Nanoclusters via Phase-Transfer Driven Ion-Pairing Reaction, *J. Am. Chem. Soc.*, 2015, **137**(5), 2128–2136.
28 L. Shen, P. Wang and Y. Ke, DNA Nanotechnology-Based Biosensors and Therapeutics, *Adv. Healthcare Mater.*, 2021, **10**(15), 2002205.
29 W. Ma, Y. Zhan, Y. Zhang, C. Mao, X. Xie and Y. Lin, The biological applications of DNA nanomaterials: current challenges and future directions, *Signal Transduction Targeted Ther.*, 2021, **6**(1), 351.
30 L. Hui, R. Bai and H. Liu, DNA-Based Nanofabrication for Nanoelectronics, *Adv. Funct. Mater.*, 2022, **32**(16), 2112331.
31 M. Xie, J. Jiang and J. Chao, DNA-Based Gold Nanoparticle Assemblies: From Structure Constructions to Sensing Applications, in *Sensors*, 2023, vol. 23.
32 D. Mathur, S. A. Díaz, N. Hildebrandt, R. D. Pensack, B. Yurke, A. Biaggne, L. Li, J. S. Melinger, M. G. Ancona, W. B. Knowlton, *et al.*, Pursuing excitonic energy transfer with programmable DNA-based optical breadboards, *Chem. Soc. Rev.*, 2023, **52**(22), 7848–7948.
33 F. Bertorelle, K. D. Wegner, M. Perić Bakulić, H. Fakhouri, C. Comby-Zerbino, A. Sagar, P. Bernadó, U. Resch-Genger, V. Bonačić-Koutecký, X. Le Guével, *et al.*, Tailoring the NIR-II Photoluminescence of Single Thiolated Au25 Nanoclusters by Selective Binding to Proteins, *Chem. – Eur. J.*, 2022, **28**(39), e202200570.
34 X. Kang, H. Chong and M. Zhu, Au25(SR)18: the captain of the great nanocluster ship, *Nanoscale*, 2018, **10**(23), 10758–10834.
35 M. F. Matus and H. Häkkinen, Understanding ligand-protected noble metal nanoclusters at work, *Nat. Rev. Mater.*, 2023, **8**(6), 372–389.
36 Q. Tang and D.-E. Jiang, Revisiting Structural Models for Au18(SR)14, *J. Phys. Chem. C*, 2015, **119**(5), 2904–2909.
37 S. Chen, S. Wang, J. Zhong, Y. Song, J. Zhang, H. Sheng, Y. Pei and M. Zhu, The Structure and Optical Properties of the [Au18(SR)14] Nanocluster, *Angew. Chem., Int. Ed.*, 2015, **54**(10), 3145–3149.
38 S. Bellon, D. Gasparutto, C. Saint-Pierre and J. Cadet, Guanine–thymine intrastrand cross-linked lesion containing oligonucleotides: from chemical synthesis to in vitro enzymatic replication, *Org. Biomol. Chem.*, 2006, **4**(20), 3831–3837.
39 D. Gasparutto, S. Da Cruz, A.-G. Bourdat, M. Jaquinod and J. Cadet, Synthesis and Biochemical Properties of Cyanuric Acid Nucleoside-Containing DNA Oligomers, *Chem. Res. Toxicol.*, 1999, **12**(7), 630–638.
40 F. Bertorelle, I. Russier-Antoine, C. Comby-Zerbino, F. Chirot, P. Dugourd, P.-F. Brevet and R. Antoine, Isomeric Effect of Mercaptobenzoic Acids on the Synthesis, Stability, and Optical Properties of Au25(MBA)18 Nanoclusters, *ACS Omega*, 2018, **3**(11), 15635–15642.
41 K. Pyo, V. D. Thanthirige, K. Kwak, P. Pandurangan, G. Ramakrishna and D. Lee, Ultrabright Luminescence from Gold Nanoclusters: Rigidifying the Au(I)–Thiolate Shell, *J. Am. Chem. Soc.*, 2015, **137**(25), 8244–8250.
42 Y. Negishi, Y. Takasugi, S. Sato, H. Yao, K. Kimura and T. Tsukuda, Kinetic Stabilization of Growing Gold Clusters by Passivation with Thiolates, *J. Phys. Chem. B*, 2006, **110**(25), 12218–12221.
43 T. Chen, Q. Yao, Y. Cao and J. Xie, Studying the Growth of Gold Nanoclusters by Sub-stoichiometric Reduction, *Cell Rep. Phys. Sci.*, 2020, **1**(9), 100206.
44 Y. Chen, M. Zhou, Q. Li, H. Gronlund and R. Jin, Isomerization-induced enhancement of luminescence in Au28(SR)20 nanoclusters, *Chem. Sci.*, 2020, **11**(31), 8176–8183.
45 Q. Yao, V. Fung, C. Sun, S. Huang, T. Chen, D.-E. Jiang, J. Y. Lee and J. Xie, Revealing isoelectronic size conversion dynamics of metal nanoclusters by a noncrystallization approach, *Nat. Commun.*, 2018, **9**(1), 1979.
46 H. Deng, K. Huang, L. Xiu, W. Sun, Q. Yao, X. Fang, X. Huang, H. A. A. Noreldeen, H. Peng, J. Xie, *et al.*, Bis-Schiff base linkage-triggered highly bright luminescence of gold nanoclusters in aqueous solution at the single-cluster level, *Nat. Commun.*, 2022, **13**(1), 3381.
47 K. Pyo, M. F. Matus, S. Malola, E. Hulkko, J. Alaranta, T. Lahtinen, H. Häkkinen and M. Pettersson, Tailoring the interaction between a gold nanocluster and a fluorescent dye by cluster size: creating a toolbox of range-adjustable pH sensors, *Nanoscale Adv.*, 2022, **4**(21), 4579–4588.
48 G. Schneider, G. Decher, N. Nerambourg, R. Praho, M. H. V. Werts and M. Blanchard-Desce, Distance-Dependent Fluorescence Quenching on Gold Nanoparticles Ensheathed with Layer-by-Layer Assembled Polyelectrolytes, *Nano Lett.*, 2006, **6**(3), 530–536.
49 T. Li, H. Zhu and Z. Wu, Viewing Aggregation-Induced Emission of Metal Nanoclusters from Design Strategies to Applications, in *Nanomaterials*, 2023, vol. 13.
50 Z. Wu, Q. Yao, O. J. H. Chai, N. Ding, W. Xu, S. Zang and J. Xie, Unraveling the Impact of Gold(I)–Thiolate Motifs on the Aggregation-Induced Emission of Gold Nanoclusters, *Angew. Chem., Int. Ed.*, 2020, **59**(25), 9934–9939.
51 S. Moro, M. Omrani, S. Erbek, M. Jourdan, C. I. Vandekerckhove, C. Nogier, L. Vanwonterghem, M.-C. Molina, P. Bernadó, A. Thureau, *et al.*, Self-Assembled Peptide-Gold Nanoclusters with SiRNA Targeting Telomeric Response to Enhance Radiosensitivity in Lung Cancer Cells, *Small Sci.*, 2025, **5**(2), 2400156.